Peer-reviewed version available at *Energies* **2019**, *12*, 2102; doi:10.3390/en12112102

Article

Investigation of Laminar-Turbulent Transition on a Rotating Wind Turbine Blade of Multi Megawatt Class with Thermography and a Microphone Array

Torben Reichstein [1,‡], Alois Peter Schaffarczyk [1,†,‡], Christoph Dollinger [2,‡], Nicolas Balaresque [3,‡], Erich Schülein [4,‡] Clemens Jauch [5,‡] and Andreas Fischer [2,‡]

1 Kiel University of Applied Sciences, Kiel, Germany
2 University of Bremen, Bremen Institute for Metrology, Automation and Quality Science, Bremen, Germany
3 Deutsche WindGuard Engineering GmbH, Bremerhaven, Germany
4 DLR, German Aerospace Center, Institute of Aerodynamics and Flow Technology, Göttingen, Germany
5 Flensburg University of Applied Sciences, Flensburg, Germany
* Correspondence: Alois.Schaffarczyk@FH-Kiel.de
† corresponding author
‡ These authors contributed equally to this work.

Version April 18, 2019 submitted to Energies

Abstract: Knowledge about laminar-turbulent transition on operating multi-megawatt wind turbine blades needs sophisticated equipment like hot-films or microphone arrays. Contrarily thermographic pictures can easily be taken from the ground and temperature differences indicate different states of the boundary layer. The accuracy however, still is an open question, so that an aerodynamic glove known from experimental research on aero-planes was used to classify the boundary-layer state of a 2 megawatt wind turbine blade operating in the orthern part of Schleswig-Holstein, Germany. State-of-the-art equipment for measurering static surface pressure was used for monitoring the lift distribution. To distinguish laminar and turbulent parts of the boundary layer (suction side only) 48 microphones were applied together with ground-based thermographic cameras from two teams. Additionally, an optical camera mounted on the hub was used to survey vibrations. During start-up (from 0 to 9 rpm) extended, but irregularly shaped regions of a laminar boundary layer were observed which had the same extension measured both with microphones and Thermography. When an approximately constant rotor rotation (9 rpm corresponding to approximately 6 m/s wind-speed) was achieved, a flow transition was visible at the expected position of 40 % chord length on the rotor blade, which was fouled with dense turbulent wedges and an almost complete turbulent state on the glove was detected. In all observations, quantitative determination of the flow transition positions from thermography and microphones agree well within their accuracy.

Keywords: Boundary Layer Transition, Wind Turbine, Thermography, Aerodynamic Glove

1. Introduction

Wind energy [1] has been very successful over the last years with more than 50 GW newly added rated wind power each year. One important part in any design of wind turbines especially for wind turbine blades is aerodynamics [2]. It consists of defining chord, twist and appropriate 2D aerofoil sections. From inviscid fluid mechanics it is well-known that design rules, if formulated in terms of circulation, only give expressions for $c \cdot c_L$ (chord times lift coefficient). As so-called profile losses can be estimated by 1.5 tip-speed-ratio / lift-to-drag [2] those with low drag are particularly interesting. From aeroplanes laminar aerofoils [3] are known and widely used to reduce fuel consumption during cruise flight and it is tempting to use these kind of aerofoils for wind turbines as well. A so-called operating-

Peer-reviewed version available at Energies 2019, 12, 2102; doi:10.3390/en12112102

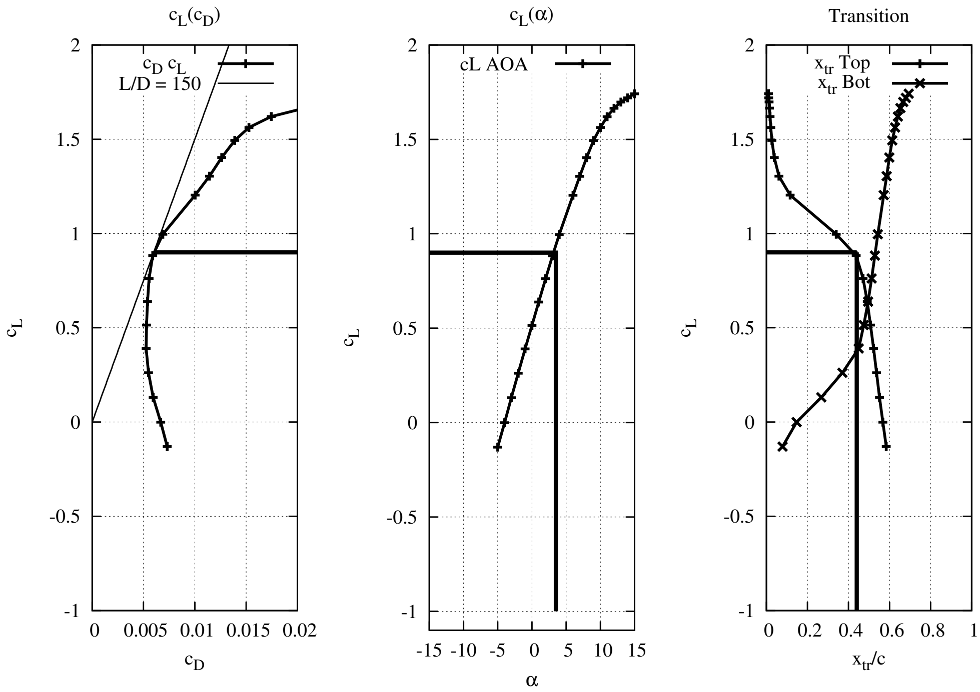

Figure 1. Determination of an operating point for an aerodynamic profile. See table 1 for numbers.

or design-point ($\alpha_{des}, c_{L,des}$) is found by constructing a tangent from the origin of the coordinate system to the $c_L(c_D)$ curve to reach for maximum lift over drag (c_l/c_d =L2D), see Figs. 1. Data calculated by Xfoil for aerofoil profile is shown in Fig. 1 and is summarised in Tab. 1. The aerofoil profile can be

Table 1. Operation point for profile at R = 35

Quantity	Value	Unit
$c_{L,des}$	0.9	-
$c_{D,min}$	0.005	-
Maximum lift over drag (L2D)	150	-
angle-of-attack	3.5	deg
laminar part (suction or top side)	0.45	x/c

found at a radius of R = 35 m on the investigated wind turbine rotor. Usually a newly designed aerofoil has to be tested in a wind tunnel. See [4] for an impressive example of high-Reynolds-number wind tunnel testing and comparison with computational fluid dynamics (CFD). Panel-codes like Xfoil as well as genuine CFD-codes like DLR-TAU [5] were used. Here, Reynolds-number and inflow turbulence level were varied and both effects could be well simulated. Furthermore, measured results agreed up to few percent in lift-to-drag ratio.

As for an aeroplane and much more pronounced for wind turbines, ambient conditions may differ substantially, especially with regard to inflow turbulence from wind tunnel settings. Therefore field tests are more or less inevitable. In fact one of the authors of this paper was inspired by [6] for a comparable experiment on wind turbine blades. In [7] a state-of-the-art version of an aerodynamic glove used on a small aeroplane is described. Unfortunately this state of sophistication in measurement equipment is not reached - at the moment - for wind turbine blades.

First investigation with emphasis on laminar-turbulent transition in the boundary layer are reported from the Energy research Centre of the Netherlands (ECN) (now part of the Netherlands Organisation for Applied Scientific Research (TNO) [8,9] for a 12-meter long blade. Much later the wind

Peer-reviewed version available at *Energies* **2019**, *12*, 2102; doi:10.3390/en12112102

energy department of the Danish Technical University (DTU) [10–12] investigated transition on a 38.8 m blade. A much more in-depth investigation is part of the current IEAwind Task 29 trans-European project [13].

A blade of 14 meter length was investigated with respect to laminar-turbulent transition by using of hot-films by [14–16]. Tab. 2 summarises all published measurements of conducted and reported laminar-turbulent transition measurements in field experiments. Nevertheless, an open question remains concerning the mechanism of transition (triggered by Tollmien-Schlichting waves or by the so-called bypass mechanism) and the accuracy of the detection of the location. This paper focuses on results from the most recent experiment on a 45.3 meter long blade and by combining two different methods (thermographic imaging and microphones) we establish quantitative reliabilty of both methods-

The structure is as following: Firstly we describe the site, the wind turbine used, its blade and the measurement equipment. Then, a summary of 2D- and 3D-CFD investigations is presented. Results are reported for pressure distribution, sound-pressure-level (SPL) in combination with thermographic pictures. Finally a summary and some conclusions are given. The paper is finalised by our conclusions and an outlook to possible further research.

Table 2. Summary of field experiments on wind turbine blades dedicated to investigations of laminar to turbulent transition

blade length/meter	year	Reynolds number/million	source
12.05	1983	3 (estimated)	[9]
38.5	2009	3 -5	[11]
14.5	2011	1 -2	[15]
2.2	2014	0.5 - 1	[17]
45.3	2018	1 - 5	this paper

2. Experimental Set-Up

2.1. Aerodynamic glove

Turbine and Site

The measurements were performed at a Senvion (formerly: REpower) MM92 wind turbine. This wind turbine has a rated power of 2 MW at rated wind speed of 12.5 m/s and the hub height is 100 m. This type of a wind turbine was firstly delivered in 2005 and since then more than 3000 units have been manufactured. The rotor blades are of type LM45.3p. Due to a non-disclosure agreement with the blade manufacturer LM, we obtained a Computer Aided Design (CAD) file of the blade's outer surface which allowed CFD simulations of the blade for comparison with the measurements.

The test site is located at Eggebek, a former military airport, approximately 100 km to the North of Hamburg and approximately 50 km to both the north Sea (to the west) and Baltic Sea (to the east). According to the European Wind Atlas[18] the roughness class is 1.5. If a logarithmic wind profile is fitted then $z_0 = 0.055$ m has to be used as roughness length. Assuming a wind speed of 6 m/s the difference by wind-shear from $z_1 = 65$ m (glove at bottom position) to $z_2 = 135$ m (glove at top position) then is 0.38 m/s or 6.3% only. Data acquisition took place on 13 July 2018 from 9 a.m. to approximately 1 p.m. local time.

Overview of the Experimental Set-Up

The experimental set up consists of different measuring techniques. First, an aerodynamic glove is used for measuring the pressure distribution and the acoustic properties of the boundary layer together with environmental parameters like temperature, humidity and local acceleration of the glove. In addition, a five hole probe is mounted onto the glove to determine the local flow velocity. Second, thermographic flow visualization was applied by two teams (Deutsche WindGuard Engineering, DWGE together with Bremer Institute for Metrology, Automation and Quality Science, BIMAQ, and German Aerospace Center, DLR) to optically determine the laminar-turbulent transition of the boundary layer. The thermographic set-ups are described in detail in section 2.2.0.1

In addition, a video camera was installed at the spinner and directed at the aerodynamic glove to measure vibrations of the blade.

Furthermore, the SCADA data from the wind turbine were given to us for a complete data set during the measurement period. All clock-times given in this article refer to local wind turbine (SCADA) time.

Aerodynamic glove

The principle of the aerodynamic glove is well known in aviation experiments for measuring the local flow conditions around the wings of an airplane [6]. For wind turbine measurements, only a few experiments were conducted [10,11,16,19,20]. For this study, a local company that is specialized in wind turbine maintenance, was commissioned to build the outer shell of the glove.

The surface consists of carbon fiber fabrics, laminated onto 20 mm thick foam plates that were aligned to a blade that is identical to the investigated one to ensure the best fit possible. The foam plates allow the installation of tubes and cables in trenches below the glove's surface without damaging the blade while maintaining the blade's profile.

In order to determine the local condition of the boundary layer, i.e., laminar or turbulent, 48 microphones were equally spaced along a straight line with an inclination of 20 degrees with respect to the chord to minimize the influence of microphones upstream. Four microphones were positioned on the pressure side, one at the leading edge of the glove and the remaining 43 on the suction side.

For the determination of the pressure distribution along the suction side, 57 pressure holes were drilled into the glove. 48 holes were distributed exactly like the microphones and the remaining nine holes were drilled at the center between two holes at the front of the glove resulting in a higher spatial resolution around the leading edge of the glove. For the acquisition of the pressure data a DTC (Digital Temperature Compensation) Initium from Esterline Pressure System was used. Fig. 2 shows the distribution of measurement points along the profile of the glove. The local flow velocity is

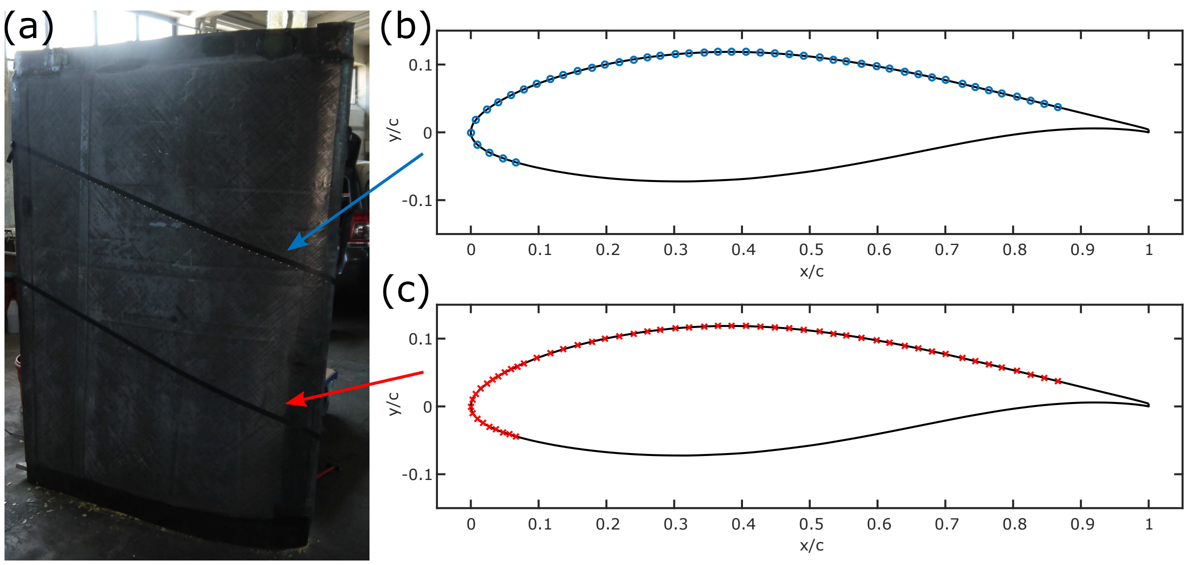

Figure 2. Position of sensors: (a) positions on the glove; (b) position of microphones; (c) positions of pressure holes

Preprints (www.preprints.org) | NOT PEER-REVIEWED | Posted: 19 April 2019 doi:10.20944/preprints201904.0225.v1

Peer-reviewed version available at Energies 2019, 12, 2102; doi:10.3390/en12112102

measured by a five hole probe. The data is also recorded by the Initium system. The five hole probe was calibrated in the wind tunnel of the University of Oldenburg, Germany.

For the data acquisition, a fan-less computer was used. It was equipped with a wifi access point to allow control of the system from the ground. The microphone data was recorded at 25 kHz and stored locally on four solid-state disks (SSD). Acceleration, temperature and humidity were also recorded at 25 kHz and stored on a separate SSD. The Initium data was recorded at 250 Hz and stored on the internal SSD of the computer via a LabVIEW program. This program was also used to synchronize all measurements. The power supply was realized by a battery with 24 V and 30 Ah. Fig. 3 shows the data acquisition system mounted on an aluminum plate ready to be mounted onto the pressure side of the glove. Obviously, there is an influence of the box on the pressure side on the flow of the suction which was investigated. Using 2D and 3D CFD (see section 3), we were able to investigate the different pressure distribution on the suction side. The differences seen there were within the accuracy of the observed values, see Fig. 11.

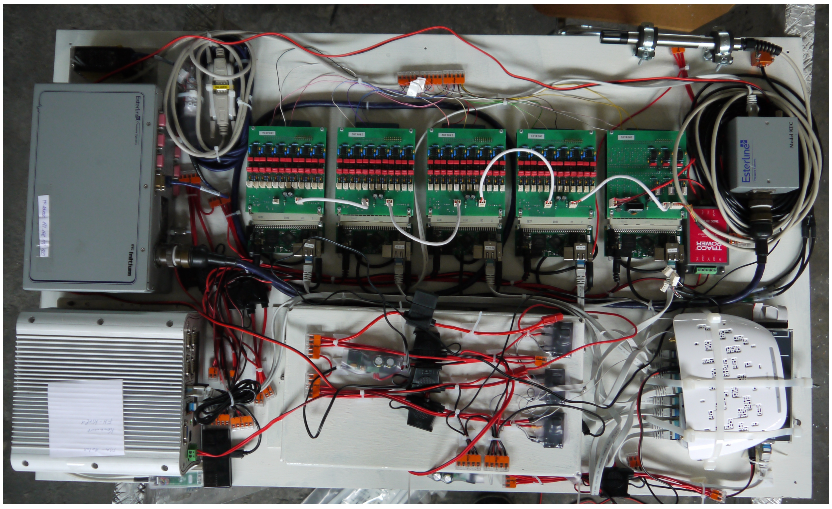

Figure 3. data acquisition system. Length about 1 meter

2.2. Thermography

A thermographic measurement of the rotor blade surface enables a non-invasive spatial resolved determination of the boundary layer state. The thermographic flow visualization relies on an initial temperature difference between the rotor blade and the flow. The rotor blade surface temperature depends on the local heat transfer coefficient which is a function of the surface friction in the different areas of the boundary layer flow [21,22]. As a result, the surface areas with a laminar boundary layer flow appear warmer than surface areas with a turbulent boundary layer flow. The transition from laminar to turbulent flow can be determined by a steep change in surface temperature. Image processing algorithms enable the localization of the laminar-turbulent transition and any existing flow separations [23–25].

Thermographic measurements have been established in wind tunnel experiments for decades to visualize the boundary layer state in ultra- and hyper-sonic as well as in trans- and subsonic flows [26]. In wind tunnel experiments the position of the laminar-turbulent transition as well as areas with laminar or turbulent flow separation can be visualized [27,28]. Outside the wind tunnel, thermographic measurements for the localization of the laminar-turbulent transition in flight experiments on aircraft wings [29], helicopter rotors [30] and wind turbine rotor blades in operation [31] are reported.

In this study different thermographic cameras were used in order to determine the laminar-turbulent transition on the aerodynamic glove and to assign the position to the three-dimensional geometry. This allows a comparison with the other sensors by chord-based position information.

Preprints (www.preprints.org) | NOT PEER-REVIEWED | Posted: 19 April 2019 doi:10.20944/preprints201904.0225.v1

Peer-reviewed version available at *Energies* **2019**, *12*, 2102; doi:10.3390/en12112102

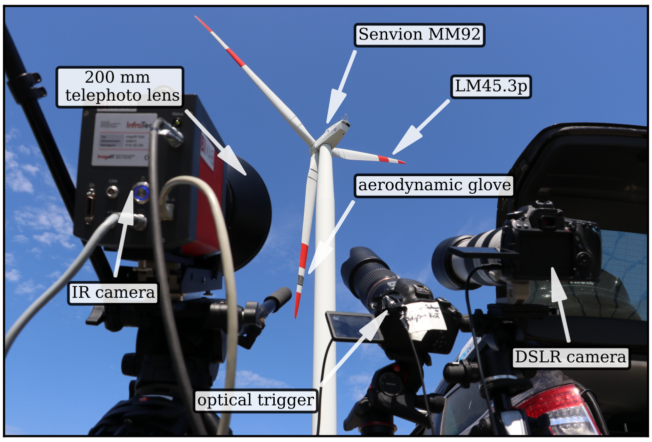

Figure 4. Experimental set-up for the thermographic flow visualization measurements. In the foreground the thermographic camera with the 200 mm telephoto lens, the optical trigger and a DSLR-camera for documentation purposes are shown.

144 Thermographic set-up provided by BIMAQ and DWGE

The thermographic measurements were acquired with a cooled thermographic camera with a global shutter (snap-shot detector) from the manufacturer InfraTec. The detector is an InSb focal plane array with 640 × 512 pixels which is sensitive between 2 and 5 μm (model ImageIR 8300). The dynamic range of the camera is 14 bit and the integration time can be set between 1 and 20,000 μs. InfraTec specifies the noise equivalent temperature difference (NETD) as less than 25 mK @ 30 °C after a standard calibration routine with measurements of a black body radiator at different temperatures. For the presented measurements a one point non-uniformity correction is performed before the measurements. A 200 mm telephoto lens with a instantaneous field of view (IFOV) of 0.08 mrad is used. This results in a spatial resolution 11.2 mm for the given measurement distance of 140 m. The thermographic camera is triggered by an optical trigger mechanism to enable the acquisition of an image every time one of the blades is passing the camera's field of view. The post-processing of the images is done in Python. Fig. 4 shows the experimental set-up for the thermographic measurements at the Senvion wind turbine.

The signal processing for the localization of the laminar-turbulent is based on the approximation of the chord wise temperature profile with a Gaussian error function, which results in a determination of the transition position with subpixel accuracy [24]. By taking into account the position of the aerodynamic glove in relation to the thermographic camera, the visible surface area can be assigned to its geometry. With the known measurement distance and the local rotor blade angle, a series of coordinate transformations is carried out to enable the determination of the angle of aperture that results in the imaging of the investigated surface in the thermographic image. The consideration of the position of the transition in the image plane of the thermographic image allows the determination of the transition position on the surface of the aerodynamic glove and subsequently the projection of this position onto the rotor blade chord [31].

Thermographic setup provided by DLR

The second infrared camera set-up was provided by the German Aerospace Center (DLR) and installed at a sufficient distance of approx. 80-85 m downstream of the wind-turbine mast to have an unobstructed view of the suction side of the aerodynamic glove at the minimum height above the ground level (Fig. 5). Thermal images taken shortly before the blade disappears behind the mast offer the best possible spatial resolution at given test conditions. Moreover, any distracting sunshine reflections can simply be avoided by this way due to nearly vertical blade alignment.

Preprints (www.preprints.org) | NOT PEER-REVIEWED | Posted: 19 April 2019 doi:10.20944/preprints201904.0225.v1

Peer-reviewed version available at Energies 2019, 12, 2102; doi:10.3390/en12112102

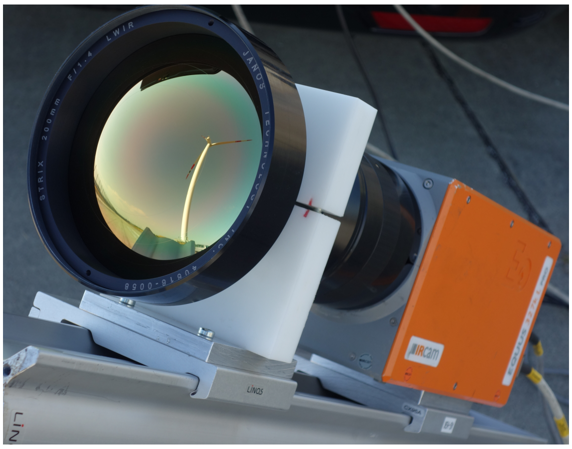

Figure 5. Thermographic setup provided by DLR: thermographic *IRCAM Equus 327k L MCT* camera equipped with a *STRIX 200mm LWIR* telephoto lens

The measurements were conducted with the *IRCAM Equus 327k L MCT* camera, which has a spectral range of 8.0-9.4 μm detected by a Cadmium-Mercury-Telluride FPA-detector with 640×512 pixels (pixel pitch: 24μm). The nominal exposure time of 100 μs at highest frame rate of 105 Hz in free-running mode was applied without image triggering or averaging. To improve spatial resolution an infrared *STRIX 200 mm LWIR* telephoto lens with a focal length of 200mm and a lens aperture of F/1.4 was used enabling a maximum resolution of approx. 125 pixel per chord width (= 83.3 px/m or 12 mm/px). This spatial resolution is marginally satisfactory for transition detection. A higher spatial resolution is simply invaluable at these long distances, because the prices for IR lenses are increasing exponentially with the focal length. The temperature difference between the glove surface and the flow needed for the transition detection was facilitated by naturally preheating the blades in the sunshine.

2.3. Optical camera

At the spinner of the WT, a video camera was mounted and directed towards the pressure side of the aerodynamic glove. Due to the curvature of the blade, it was not possible to observe the suction side of the glove. The camera was intended to visually detect vibrations of the blade, which in turn could be correlated to oscillations of the local acceleration. Potential disturbance from precipitation, insects or birds could be observed. Heating up of the blade and the aerodynamic glove from varying sun radiation could be assessed, also in the blade positions that are out of sight for the stationary thermographic cameras. The optical camera is a JVC GZ-RX115BE camcorder. The camera was mounted onto the spinner with a rack that keeps the camera firmly in place. Contained in this rack is also an additional battery pack that allows about 24 hours of continuous operation. The camera is not remotely controlled. Instead the recording is started before the WT is started and the camera records during the whole test. The optical camera records with a rate of 50 frames per second. The resolution of the pictures is 1920 x 1080 pixels. Fig. 6 shows that in standstill of the WT (pitch angle approx. 90 deg) the camera points towards the pressure side of the blade. In operation at low wind speeds (pitch angle approx. 0 deg) the camera points towards the trailing edge and the pressure side of the blade. At low pitch angles the spoiler on the pressure side of the blade root becomes visible. Since the blade is flexible the view varies with the out of plane bending of the blade (driven by thrust forces) and the in-plane bending of the blade (mainly driven by the gravitational force, i.e. determined by the rotor position). The optical camera has a focal length range from 2.9 mm to 116 mm. Therefore, the aerodynamic glove could have been observed a lot closer. However, the intention was to observe also the blade around the aerodynamic glove. The high resolution of the pictures allows zooming into the videos if necessary for assessing certain scenarios, for example during start-up phase.

Preprints (www.preprints.org) | NOT PEER-REVIEWED | Posted: 19 April 2019 doi:10.20944/preprints201904.0225.v1

Peer-reviewed version available at Energies 2019, 12, 2102; doi:10.3390/en12112102

Figure 6. View from the optical camera on the spinner to the pressure side of the blade at R = 35 m. The black box contains all the data recording system including power supply. Chord there is 1.5 m. In addition, orientation of the 5-hole-probe relative to vertical axis (approx. rotor plane) indicates the instantaneous pitch to be compared with values from the SCADA system. Left: WT in standstill, right: WT in operation.

3. Computational Fluid Dynamics

Parallel to the preparation of the experiments, 2D and 3D CFD simulations were performed. First, a 2D simulation was performed using XFOIL [32]. In Fig. 7 the resulting Lilienthal polar of that section is shown. A so-called laminar nose, a region of small drag, $c_D < 0.008$, is clearly visible. Using a tangent, the operating point of the airfoil ($\alpha_{des}, c_{L,des}$) is determined at the largest lift-to-drag ratio $c_{L,des}/c_{D,des}$. Fig. 8 and 9,right side show the (2D-)pressure distribution on the surface of the profile for an angle of attack of $\alpha_{des} = 3.5°$ at operating conditions. It is clearly seen that no flow separation is present there. It has to be noted, that for every CFD calculation including laminar to turbulent transition an additionally quantity, the N-factor has to be provided. From wind tunnel measurements it is common practice to relate N to the inflow turbulence TI by Mack's relation

$$N = 2.13 - 6.18 \cdot \log_{10}(TI) \; . \tag{1}$$

Mack [33,34] recommended to use it in the region $0.1\% < TI < 1\%$. Here, TI comes from $TI = \sigma/\overline{v}/ = (\int v^2 P(v)dv)^{1/2} / \int vP(v)dv$, or in words: standard deviation divided by average wind speed for some ensemble. Note that Eq. 1 cannot be used in atmospheric flow without further assumptions. A procedure how to extend Mack's correlation, was proposed in [20].

Furthermore, full 3D simulations were used to estimate the position of transition from laminar to turbulent flow in the boundary layer on the suction side of the glove. Fig. 9,left shows the expected flow state regions obtained via DLR-TAU code [5], a CFD code by the German Aerospace Center. Blue corresponds to laminar flow, red indicates a fully turbulent flow. A transition line is seen around $x/c = 0.3$ (c = total chord = 1.5 m) in the central region of the glove. Due to boundary effects transition is forced more to the leading edge at the border of the glove.

In addition, the perturbation of the flow due to the box on the lower side of the glove was investigated and has been seen a posterior to be within the variation due to surface imperfections. Fig. 9, right shows the 3D-pressure distribution. Again, as for transition, the central part, where the pressure sensors and the microphones had been placed, smooth variations as expected from 2D are visible. From these investigation we can conclude that even under ideal conditions a laminar extension of the suction side not longer that 40 % can occur.

Preprints (www.preprints.org) | NOT PEER-REVIEWED | Posted: 19 April 2019 doi:10.20944/preprints201904.0225.v1

Peer-reviewed version available at Energies 2019, 12, 2102; doi:10.3390/en12112102

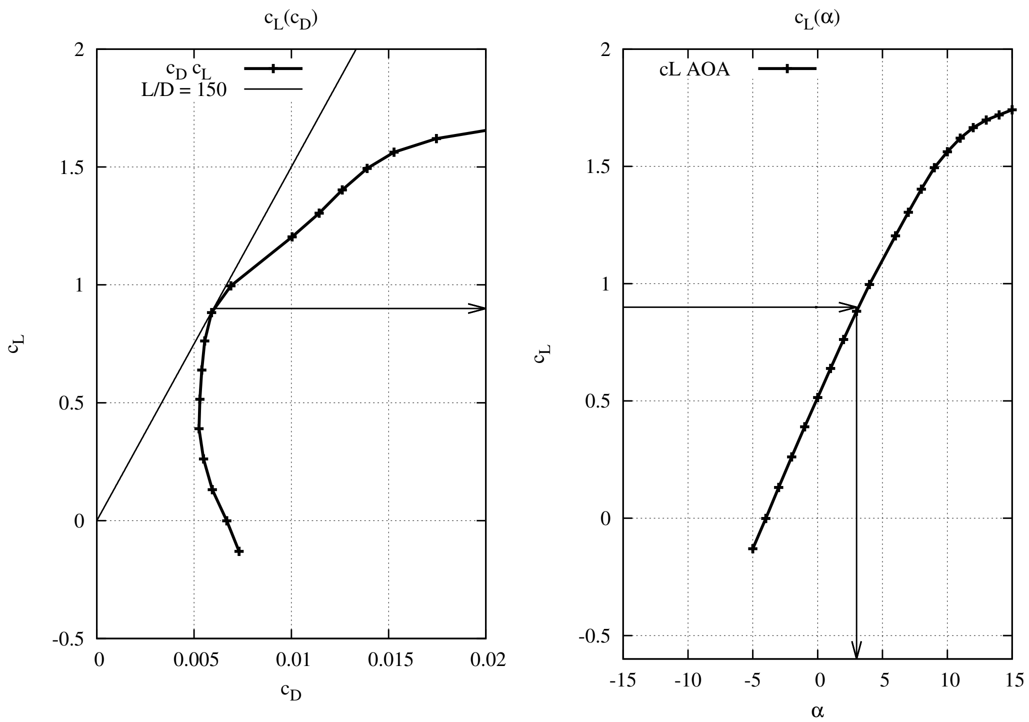

Figure 7. Lilienthal-polar of the profile at the location of the glove (Reynolds number 4 million). A so-called *laminar nose*, a region of small drag $c_d < 0.008$, is clearly visible. Arrows indicate determination of operation point using a tangent. The N-factor was chosen arbitrarily to 3. By Mack's correlation this corresponds to an inflow turbulence of 0.7%.

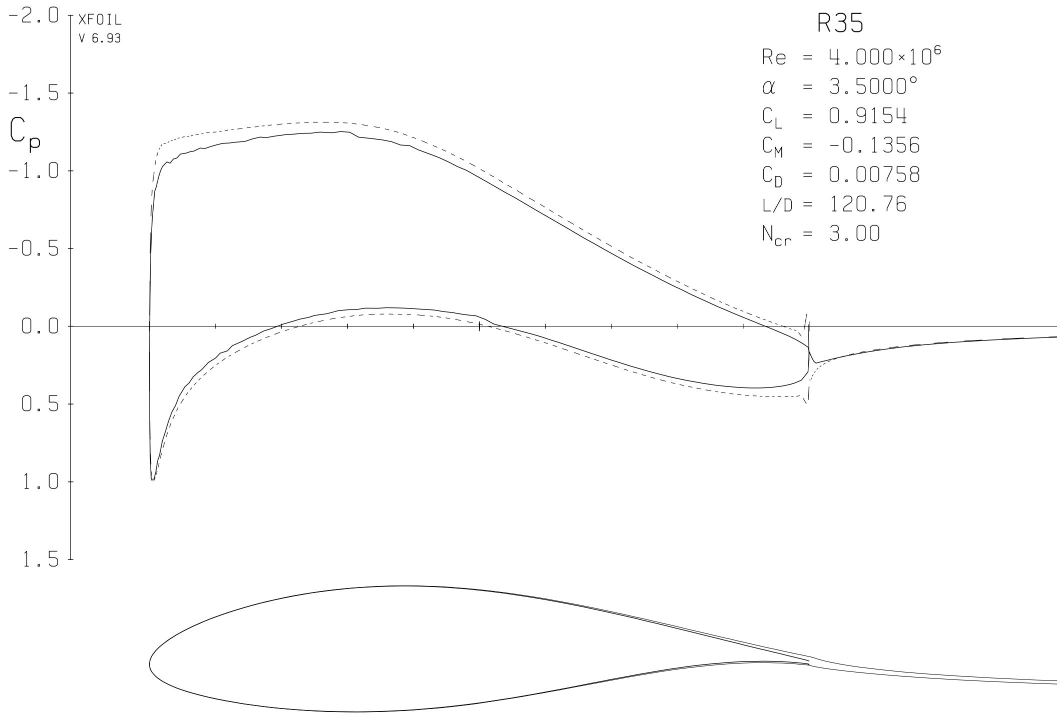

Figure 8. Static pressure on profile from Fig. 7 using Xfoil. AOA 3.5°

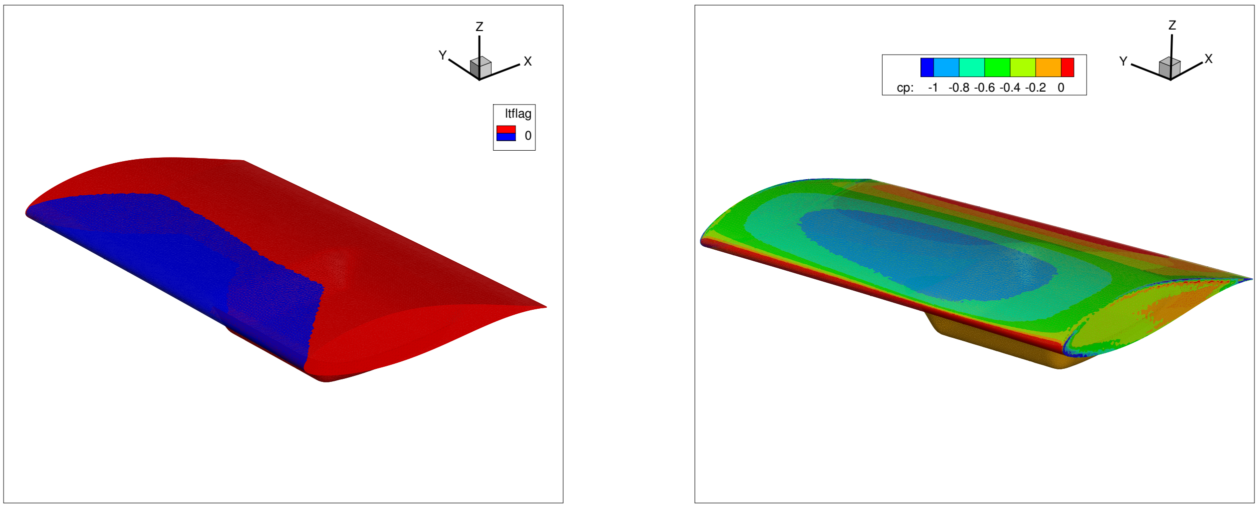

Figure 9. Left side: Estimated flow state regions from 3D transitional CFD (DFL-TAU code). Blue: laminar flow, red: fully turbulent flow. Right side: Static pressure coefficient.

Peer-reviewed version available at Energies 2019, 12, 2102; doi:10.3390/en12112102

4. Measurement results

4.1. Measurements

Now, the results are discussed in more detail in order to present a complete picture of the aerodynamic properties of the boundary layer flow around the glove.

Two different data sets are compared, the start-up (SU) of the wind turbine (dataset 11:01) and the steady-state (SS) of the wind turbine (dataset 11:18). These two data sets were chosen exemplarily to illustrate the different operation states. All measurements were performed on a single sunny day over a time period of about four hours. First, six sequences, each 60 seconds long, were recorded in a stand-still configuration with the brakes of the turbine tightened. After that, the brakes were loosened and the turbine was started. 31 sequences with 60 seconds length and a delay of 30 seconds in between were recorded. During the measurements the turbine was stopped and started again in order to measure the start-up of the turbine as well as the steady-state. The goal was to find differences between the different operation states to study the temporal evolution of the boundary flow conditions.

While the measurement system in the glove recorded data continuously, the thermography cameras recorded stationary images of the glove at a fixed position of the blade's revolution.

4.2. Inflow

First, the inflow obtained by the five hole probe is discussed. Due to the calibration of the probe in the wind tunnel of the University of Oldenburg, Germany, it was possible to obtain the inflow velocity together with the angle of attack (AOA). Fig. 10 shows both quantities of the flow for the different operation states, respectively. It can be seen that for SU the AOA is increasing from negative to positive

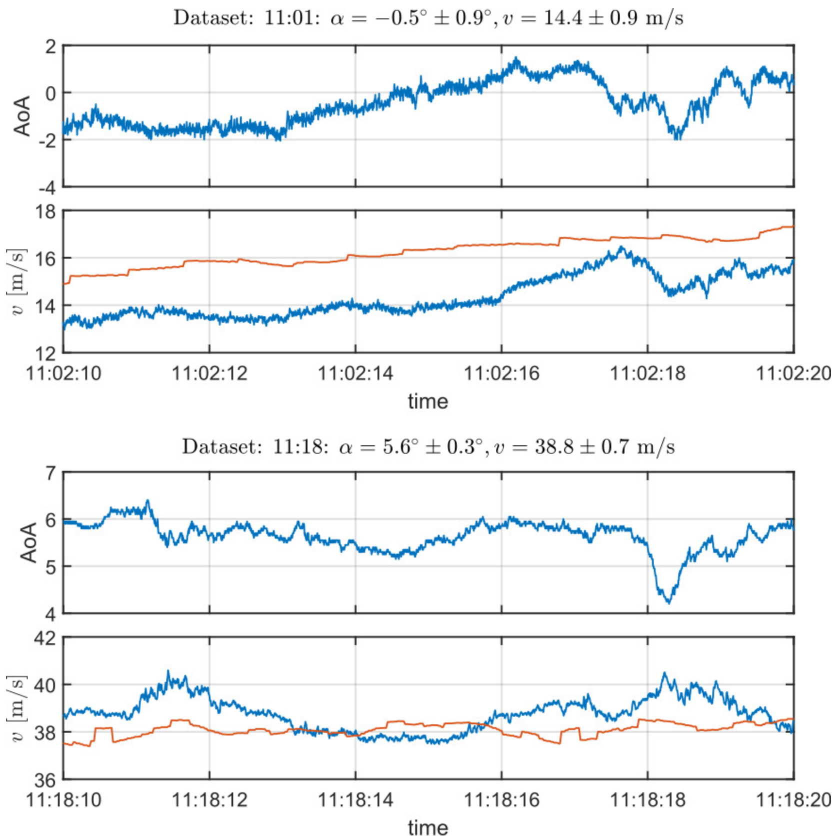

Figure 10. Inflow properties of different operation states. Top: start-up, bottom: steady-state. Shown is AOA (upper row) and inflow velocity (lower row). Blue: velocity obtained by five hole probe, red: velocity obtained by SCADA data.

Preprints (www.preprints.org) | NOT PEER-REVIEWED | Posted: 19 April 2019 doi:10.20944/preprints201904.0225.v1

Peer-reviewed version available at Energies 2019, 12, 2102; doi:10.3390/en12112102

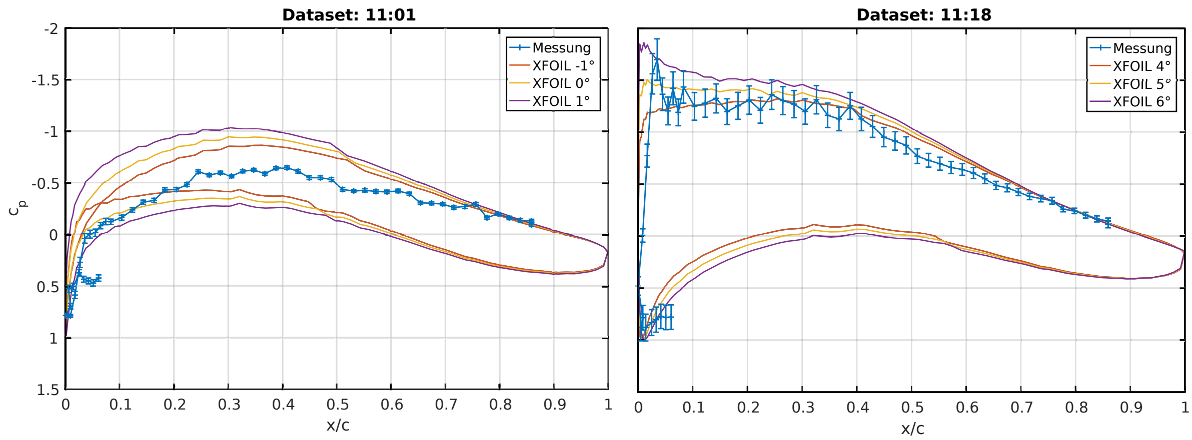

Figure 11. Pressure (c_p) distribution on the glove. Left: Start-up; right: steady-state.

values as expected. In addition, an offset between the inflow velocity obtained by the probe (blue) and by SCADA data (red) is seen which is explained by the different locations where the wind speed is measured.

For SS, the variation of the AOA is much smaller and no drift is observed. The offset between the inflow velocities is no longer observed. Furthermore, the inflow velocity varies along the revolution of the blade which is a direct confirmation of the atmospheric layering.

4.3. Pressure distribution

Furthermore, the pressure distribution on the glove was measured. For a better comparison, the same 10 s sequence as in Fig. 10 was used. The recorded pressure was averaged and using

$$c_p = \frac{2(p - p_0)}{\rho v^2} \tag{2}$$

the lift coefficient c_p was calculated. Fig. 11 shows the resulting distribution of c_p for both operating states. For comparison, the CFD results of XFOIL calculations with different AOA are also shown.

For SU, a poor agreement is found which might result from the transient character of the sequence. AOA increases from $-1°$ to $+2°$ which makes a comparison with a stationary AOA somewhat difficult.

For SS, a better agreement between measurement and CFD is observed. The measured AOA of the five hole probe of 5.6° (cf. Fig. 10) is in good agreement with the observed c_p distribution.

It is worth noting that for both states the pressure distribution on the pressure side of the glove differs from the CFD calculations. Since the pressure distribution is strongly dependent on the local curvature at the leading edge, small deviations of the glove's shape result in large changes of the lift coefficient.

Too high production costs for a glove with wind tunnel (or even commercial blade) quality prevented a smoother surface. Hence, part of the observed deviations might be explained by insuffcient surface quality.

4.4. Detection of transition position

In addition to the pressure distribution the determination of the flow character of the boundary layer was a main goal of this project. Therefore, the noise emission on the suction side was recorded by the 48 microphones.

Preprints (www.preprints.org) | NOT PEER-REVIEWED | Posted: 19 April 2019 doi:10.20944/preprints201904.0225.v1

Peer-reviewed version available at Energies 2019, 12, 2102; doi:10.3390/en12112102

The determination of the transition position was performed as described in Ref. [10]. Firstly, the power spectral density of the pressure signal form the microphones $\widetilde{p(\omega)}$ was calculated from the time-series $p(t)$ by applying

$$\widetilde{p(\omega)} := \frac{1}{2\pi} \int_{-\infty}^{+\infty} r_{pp}(t) \cdot e^{-i\omega t}\, dt\,, \tag{3}$$

$$r_{pp}(t) = \lim_{T\to\infty} \frac{1}{2T} \int_{-T}^{+T} p(\tau)p(\tau+t) \cdot d\tau\,. \tag{4}$$

assuming a real time signal. Furthermore, [10] used only a finite part of the spectrum

$$p^2_{cut} = 2 \int_{\omega_1}^{\omega_2} \widetilde{p(\omega)}\, d\omega \tag{5}$$

with $[f_1; f_2]$=[2 kHz; 6 kHz], $\omega = 2\pi f$ and $p_{ref} = 20\mu$Pa. The relevant sound pressure level (SPL) L_p^{cut} then is determined by

$$L_p^{cut} = 20 \log_{10}\left(\frac{P_{cut}}{p_{ref}}\right) (dB)\,. \tag{6}$$

By definition SPL is given in pseudo-units of dB (Decibel). In order to study the temporal evolution of the SPL, sequences of 2048 data points were averaged and the SPL for this sequence was calculated resulting a time resolution of 12 Hz. Fig. 12 shows the temporal evolution of the SPL for both operating states, together with the local radially outwards directed acceleration.

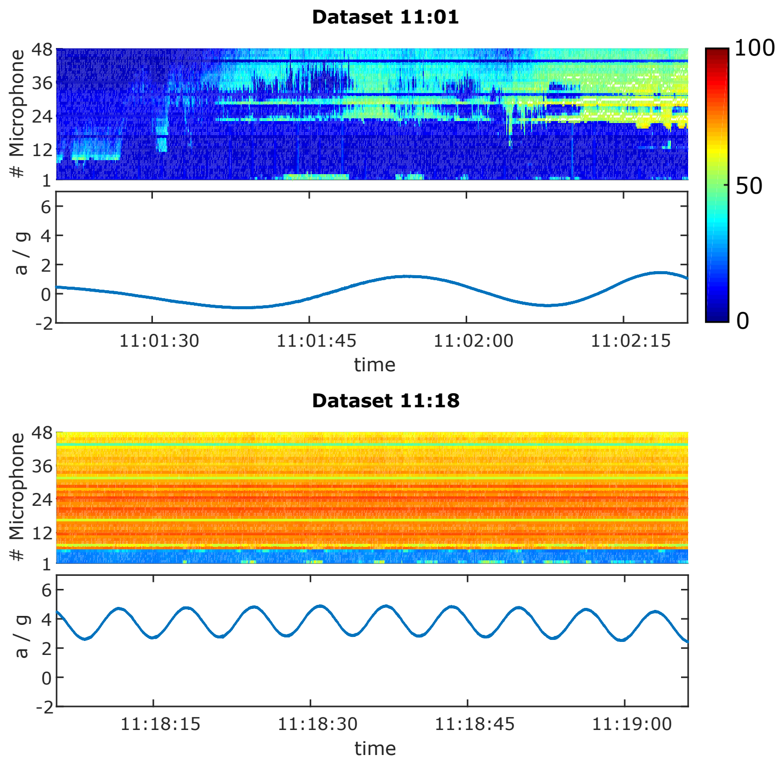

Figure 12. Detection of the transition position. Top: Start-up; bottm: steady-state. Upper row: sound pressure level in dB, Color map: Dark blue correspond to 0 dB and red to 80 dB. lower row: local acceleration.

Peer-reviewed version available at Energies 2019, 12, 2102; doi:10.3390/en12112102

The color map changes from blue via green and yellow to red with increasing values of SPL. The overall value of the SPL is lower in the SU than in the SS. Furthermore, areas with higher SPL can be found at the back part of the suction side that travel in the direction of the leading edge.

In the SS, the overall value of SPL is higher. In addition, a distinct region at the leading edge can be recognized with much lower values of SPL. This is a characteristic of a laminar boundary layer while most of the suction side has a turbulent boundary layer resulting in high values of SPL.

Furthermore, a small periodic variation of the transition position can be observed. Due to the periodic variation of the local acceleration the blade position relative to the ground can be determined. At the lowest point of the revolution gravity and centrifugal force are pointing in the same direction, resulting in a maximum acceleration. At this position, the transition position is slightly moving in direction of the leading edge. Since the blade is passing through the wind shadow of the tower a higher inflow turbulence is expected, thus resulting in a more turbulent boundary layer.

4.5. Thermography Team BIMAQ and DWGE

As an example the results from 11:15:32 and 10:16:45 (SCADA time) are shown. Fig. 13 shows the transition position derived by the image processing algorithm from Dollinger et al. [24] for the start up phase of the wind turbine. On the left side the thermographic image with the visible leading (LE) and trailing edge (TE) as well as the derived relative transition position p_{tr} are shown. On the right side, the surface temperature T of the glove at the location of the microphones is shown as a function of the position on the chord x/c determined by a previously performed geometric assignment [31]. The span wise average transition position along the glove is $\bar{x}_{tr,\,IR}/c = 0.337$ with large local fluctuations due to turbulence wedges as a result of the high surface roughness of the aerodynamic glove. Locally at the location of the microphones the transition position determined by the thermographic flow visualization is $x_{tr,\,IR}/c = 0.255 \pm 0.003$. The uncertainty of the measurement is estimated according to [31]. This result is consistent to the transition location deduced by the microphone data $x_{tr,\,M} = 0.26 \pm 0.01$ (cf. Fig. 14). In Fig. 15 the results for the turbine in regular operation mode are shown. Again, on

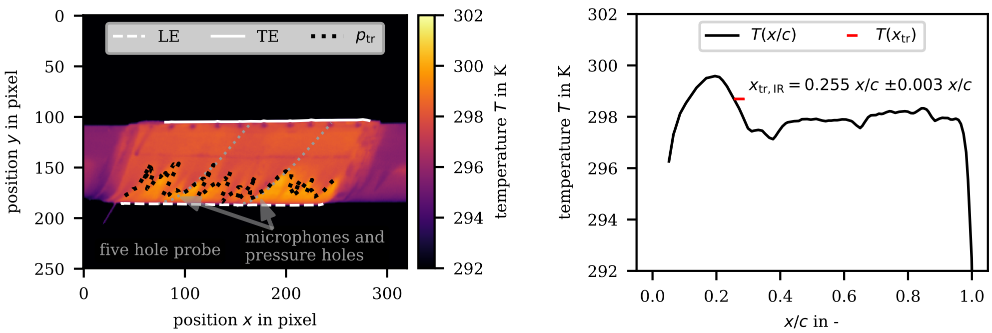

Figure 13. Thermographic flow visualization measurement at 11:15:32 (SCADA time)

the left the thermographic image of the glove is shown and on the right the surface temperature T is depicted as a function of the chord wise position x/c. Beside the relative position of the transition in the image p_{tr}, the visible leading and trailing edge are shown. Due to a reflection of sunlight on the surface of the glove, the area towards the trailing edge appears very warm. This area is not included in the image processing for the evaluation of the transition position. The span wise average transition position for this measurement is $\bar{x}_{tr,\,IR}/c = 0.048$ and the transition position at the location of the microphones is $x_{tr,\,IR}/c = 0.039 \pm 0.004$. From microphone data we here get a slightly larger value of $x_{tr,\,M}/c = 0.05 \pm 0.01$. Note that the spacing of the microphones is 0.02 (in units of x/c).

Obviously, the rough surface leads to a premature laminar-turbulent transition near the leading edge during these operational conditions.

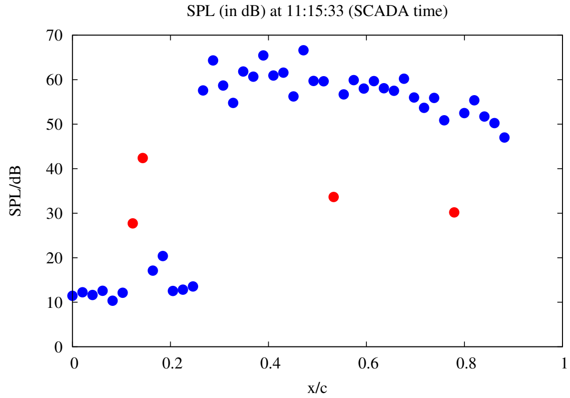

Figure 14. Development of SPL (in dB) vs chord at 11:15:32 (SCADA time). If one discards outliners (in red) $x_{\text{tr, M}}/c$ may be deduced to $x_{\text{tr, M}}/c = 0.26 \pm 0.01$

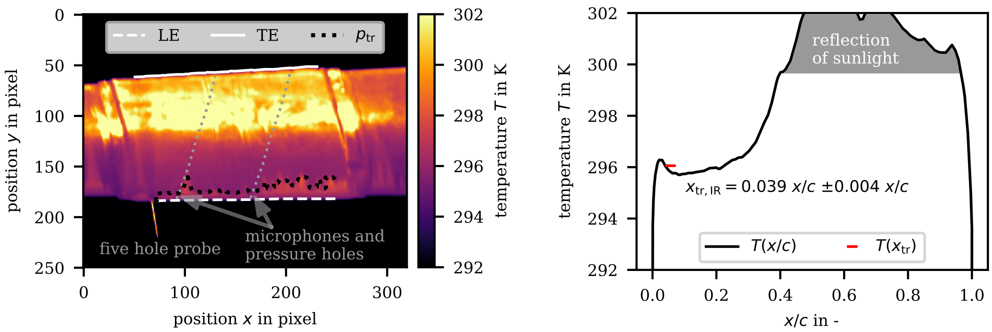

Figure 15. Thermographic flow visualization measurement at 10:16:45 (SCADA time)

4.6. Results Team DLR

As described above, the detection of boundary layer transition on rotating blades relies on the increase in the heat transfer rate between the flow and the blade surface that occurs when the boundary layer state changes from laminar to turbulent. The change in the heat transfer rate causes differences in the blade surface temperature that was measured by an infrared camera.

Thus, the transition detection was based on the analysis of single instantaneous thermal images of the rotating blade in the start up phase, indicating different stages of surface-temperature evolution from the initially quasi uniform to a final locally-equilibrium distribution. The image pre-processing includes here the bad-pixels elimination, the sky-background separation and the contrast enhancement. Fig. 16 shows two typical thermal images obtained correspondingly at 11:22:27 and 11:23:13 (SCADA time) during a single wind-turbine run preprocessed accordingly. The rotation direction is here from left to right and the cold-sky background is colored maroon to enhance the visibility of the wind-turbine parts presented in graduations of gray. The vertical gray-scaled area on the right side of the picture represents the mast of the facility. The areas with laminar (warm/bright) and turbulent (cold/dark) boundary layers on the glove surface can be clearly distinguished in these pictures. The variations of the rotation rate (from 4.0 rpm to 8.5 rpm) and of the blade pitch angle (from 20 degrees down to 1 degree) taking place between these both time instances during the start up phase causes the shifting of the transition region in time documented thereby.

In the next step the DLR software *HeatFIT* was used for the final conditioning and automatic marker-based 3D-reconstruction of the thermal images with subsequently mapping of the data values onto the 3D grid of the aerodynamic glove (Fig. 17). The geometric information necessary for the markers is provided by the CFD-model. A full computerized analysis of the temperature distribution on the test surface in accordance with the method introduced by Schülein [35] allowed the distinction

Preprints (www.preprints.org) | NOT PEER-REVIEWED | Posted: 19 April 2019 doi:10.20944/preprints201904.0225.v1

Peer-reviewed version available at Energies 2019, 12, 2102; doi:10.3390/en12112102

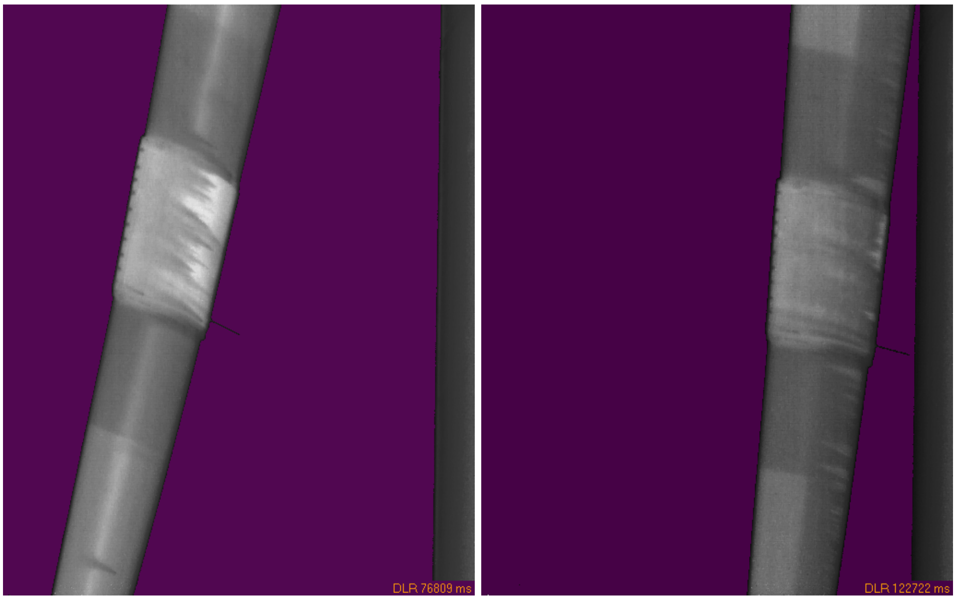

Figure 16. Two typical thermal images obtained by DLR-setup after image processing including bad-pixels elimination, sky-background replacing and contrast enhancement. Images are from 11:22:27 (left) and 11:23:13 (right, both SCADA time). The left picture shows more laminar parts during startup and the right one only very small extended regions during constant RPM (approx. 9) operation mode.

between the starting points and the end points of the transitional region. Additionally, in a simplified approach the transition zone between laminar and turbulent flows was detected as a border line, which corresponds to the locations with the highest wall-temperature gradients (highest gradients of the thermal image intensity) measured in streamline direction (areas with detected laminar flow are highlighted in yellow in Fig. 18). Fig. 19 shows a typical surface temperature distribution (here thermal image intensity) over the normalized coordinate x/c extracted from the left thermal image in Fig. 18 along the midline of the glove. This example demonstrates the mutual positions of points characterizing transition zone: onset transition, end of transition and highest temperature gradient. As described in Ref. [30] and seen in the example presented, the transition line detected in accordance with the highest-gradient criterion corresponds approximately to the midpoint of the transition zone. A comprehensive characterization of the transition zone facilitates comparison with results obtained independently by different experimental methods and numerical simulations. The actual midpoints of the transition zone detected in both thermal images along the microphone-array line were found to be at $x_{tr,IR}/c = 0.370 \pm 0.005$ and 0.080 ± 0.005, being very close to the transition locations detected by microphone-array method ($x_{tr,m}/c = 0.34 \pm 0.01$, see Fig. 20 and 0.07 ± 0.01).

4.7. Discussion

Main objective was a quantitative comparison of detection of laminar-turbulent transition positions with two different methods: Thermographic pictures and microphones. It is interesting to note that both methods agree in their results within their limitations: Thermography takes maximum temperature gradient as the *location* of transition as Figs 13 and 15 indicate. In contrast (see Fig 14) transition from SPL seems to be very sharp within one unit of distance (= 1/40 = 0.025 in terms of x/c).

If one uses CFD (see Fig. 21) to determine laminar to turbulent transition then results compare more to a region with the end of the laminar part ($(x/c)_{lam-end}$= 0.29) given by the minimum of c_f and the beginning of the fully turbulent region by the the following maximum ($(x/c)_{fully-turb-start}$= 0.42).

Therefore it can be stated that thermographic imaging provides a non-intrusive method which can be used from a distance to detect laminar to turbulent transition its accuracy proved to be in accordance with data both from microphones and transitional CFD.

Preprints (www.preprints.org) | NOT PEER-REVIEWED | Posted: 19 April 2019 doi:10.20944/preprints201904.0225.v1

Peer-reviewed version available at Energies 2019, 12, 2102; doi:10.3390/en12112102

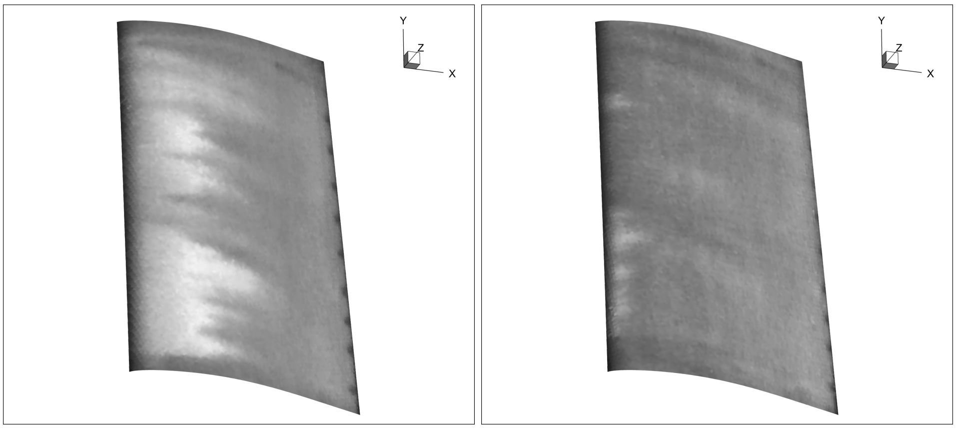

Figure 17. Thermal images from Figure 16 after reconstruction and mapping onto the 3D grid of the aerodynamic glove. Images are from 11:22:27 (left) and 11:23:13 (right, both SCADA time). Here the glove are is shown only.

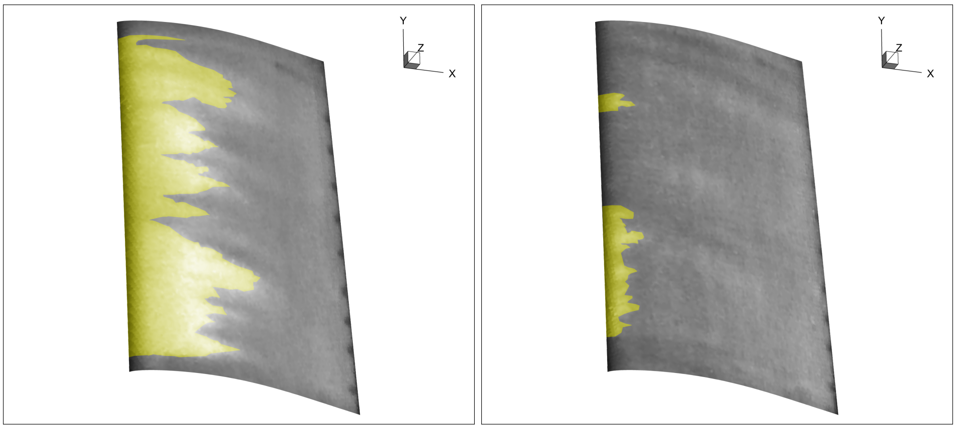

Figure 18. Thermal images from Figure 16 after transition detection procedure.

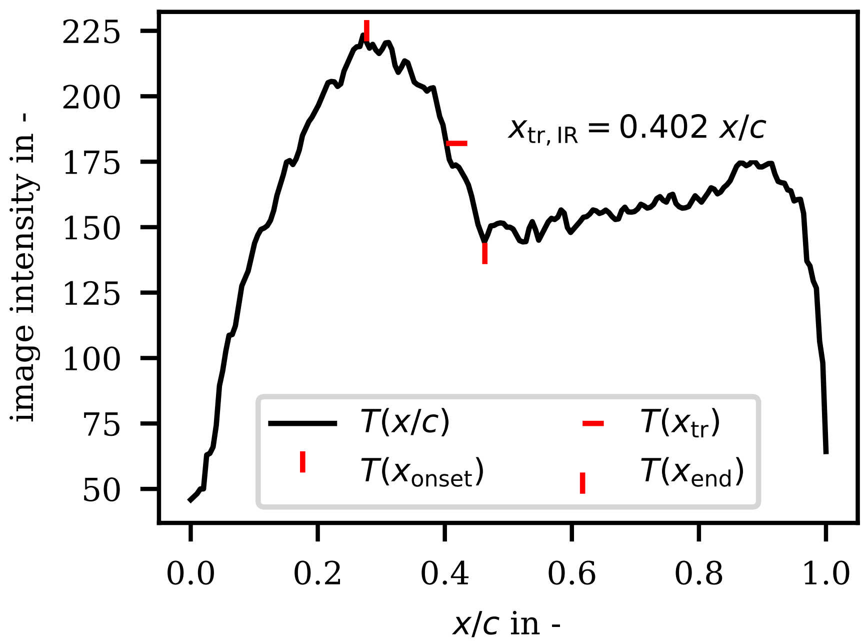

Figure 19. Thermal image intensity extracted along the microphone-array line for the time instance 11:22:27.

Preprints (www.preprints.org) | NOT PEER-REVIEWED | Posted: 19 April 2019 doi:10.20944/preprints201904.0225.v1

Peer-reviewed version available at Energies 2019, 12, 2102; doi:10.3390/en12112102

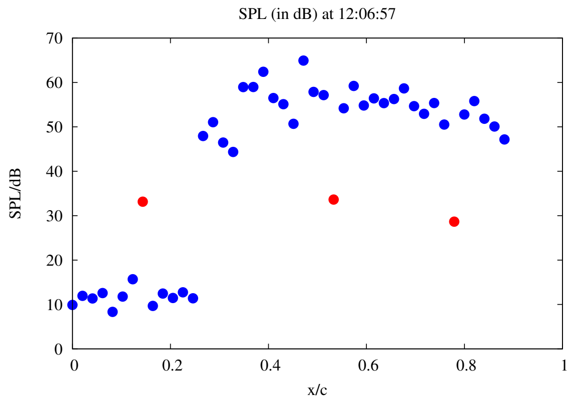

Figure 20. Development of SPL vs chord at 12:06:57. If one discards outliers (in red) $x_{\mathrm{tr,\,M}}/c$ may be deduced to $x_{\mathrm{tr,\,M}}/c = 0.34 \pm 0.01$

5. Summary and Conclusions

An aerodynamic glove known from free-flight experiments with air planes was designed, manufactured and used on a 2 MW state-of-the-art wind turbine to investigate laminar to turbulent transition. Local inflow conditions were recorded by a 5-hole-probe and surface pressure measurements were performed by an array of 64 pressure sensors from PSI-Initium. In addition an array containing 48 microphones was used for capturing flow sound near the wall. Two different types of thermographic cameras were used to report the rotor surface temperature and thereby distinguish laminar (warmer) and turbulent (colder) regions. Angle-of-attack could be determined from 5-hole probe and pressure distribution within 1 degree accuracy.

Although the geometric surface did not met standards from wind tunnel models and during the measurement blade and glove seemed to be fouled by insects and/or dust, the irregularly shaped regions of laminar boundary layer were consistently identified by thermographic imaging and microphones even during wind turbine start up and agreed within their respective accuracies.

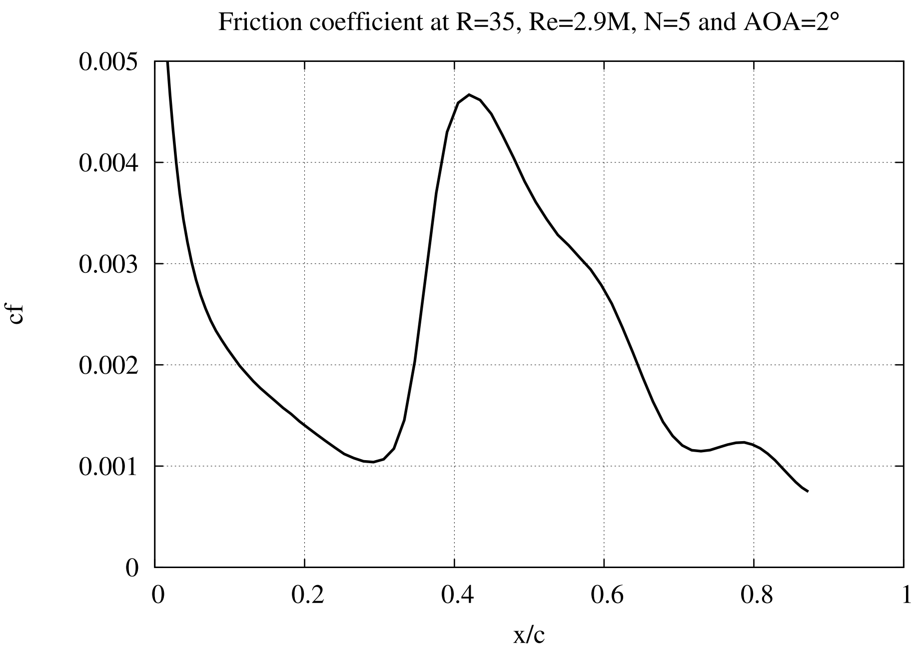

Figure 21. Location of transition from wall shear stress (c_f) by CFD-code FLOWer. *N*=5 corresponds to a turbulence intensity (*TI*) of 0.3 %. Onset of transition may be located at $x/c = 0.29$ and flow is fully turbulent at $x/c = 0.42$. Slope is at maximum at $x/c = 0.36$.

References

1. Schaffarczyk (Ed.), A. *Understanding WIND POWER TECHNOLOGY*; Wiley: Chichester, UK, 2014. doi:10.1002/9781118701492.index.
2. A.P. Schaffarczyk. *Introduction to Wind Turbine Aerodynamics*; Springer Verlag, Berlin, 2014.
3. Abbot, I.H.; von Doenhoff, A. *Theory of Wind Sections*; Dover Publications Inc.: New York, USA, 1959.
4. O.C. Yilmaz, O.P.; Munduate, X.; Sørensen, N.; Reichstein, T.; Schaffarczyk, A.; Manolesos, M.; Barakos, G.; Daniele, E.; Schwarz, M.; Lutz, T.; R.Prieto. Summary of the Blind Test Campaign to predict the High Reynolds number performance of DU00-W-210 airfoil. AiAA SciTech Forum, Grapevine, TX, USA, 2017.
5. TAU-Code User Guide, Release 2018.1.0. Technical report, Deutsches Zentrum für Luft- und Raumfahrt e.V., Institute of Aerodynamics and Flow Technology, July 10, 2018.
6. Seitz, A.; Horstmann, K.H. In-flight investigation of Tollmien-Schlichting waves. IUTAM Symposium on One Hundret Years of Boundary Layer Research; Meier, G.; Sreenivasan, K., Eds., 2006, pp. 115–124.
7. Reeh, A.; Tropea, C. Behaviour of a natural laminar flow airfoil in flight through atmospheric turbulence. *Journal of Fluid Mechanics* **2015**, *767*, 394–429. doi:10.1017/jfm.2015.49.
8. van Groenewoud, G.J.H and Boermans, L.M.M and van Ingen, J.L. Onderzoek naar de omslag laminar-turbulent van de grensllag op de rotorblades van de 25 m HAT windturbine. Rapport LR-390, Technische Hogeschool Delft, 1983.
9. J.L. van Ingen and J.G. Schepers. Prediction of boundary layer transition on the wind turbine blades using th e^N method and a comparison with experiment. priv comm.
10. Troldborg, N.; Bak, C.; Aagaard Madsen, H.; Skrzypinski, W. *DANAERO MW: Final Report*; DTU Wind Energy: Denmark, 2013.
11. Madsen, H.; Fuglsang, P.; Romblad, J.; Enevoldsen, P.; Laursen, J.; Jensen, L.; Bak, C.; Paulsen, U.; Gaunaa, M.; Soerensen, N.N.; N.A., O. The DAN-AERO MW Experiments. 48th AIAA Aerospace Science Meeting Including the New Horizons Forum and Aerospace Exposition, Aerospace Science Meetings, 2010.
12. Madsen, H.A.; Özçakman Ö. S..; Bak, C.; N., T.; N., S.N.; N., S.J. Transition characteristics measuremd on a 2 MW 80 m diameter wind turbine rotor in comparison with transition data from wind tunnel measurements. AIAA Scitech Forum, 2019.
13. IEA Wind Task 29, https://community.ieawind.org/task29/home.
14. Schwab, D.; Ingwersen, S.; Schaffarczyk, A.; Breuer, M. Aerodynamic Boundary Layer Investigation on a Wind Turbine Blade under Real Conditions. Wind Energy - Impact of Turbulence; Hölling, M.; Peinke, J.; Ivanell, S., Eds.; Springer Berlin Heidelberg: Berlin, Heidelberg, 2014; pp. 203–208.
15. Schaffarczyk, A.P.; Schwab, D.; Breuer, M. Experimental detection of laminar-turbulent transition on a rotating wind turbine blade in the free atmosphere. *Wind Energy* **2017**, *20*, 211–220.
16. Schwab, D. Aerodynamische Grenzschichtuntersuchungen an einem Windturbinenblatt im Feldversuch. PhD thesis, Helmut-Schmidt-Univesität, Universität der Bundeswehr Hamburg, Hamburg, Germany, 2018. in German.
17. Schaffarczyk, A.; Boisard, R.; Boorsma, K.; Dose, B.; Lienard, C.; Madsen, T.L.H.Å.; Rahimi, H.; Reichstein, T.; Schepers, G.; Sørensen, N.; Stoevesand, B.; Weihing, P. Comparison od 3D transitional CFD simulations for rotating wings with measurements. The Science of Making Torque from Wind; , 2018.
18. Troen, I.; Lundtang Petersen, E. European Wind Atlas. Technical report, Risø National Laboratory, Rosklilde, Denmark, 1989.
19. Schaffarczyk, A.P.; Schwab, D.; Ingwersen, S.; Breuer, M. Pressure and hot-film measurements on a wind turbine blade operating in the atmosphere. *Journal of Physics: Conference Series* **2014**, *555*, 012092.
20. Schaffarczyk, A.; Schwab, D.; Breuer, M. Experimental Detection of Laminar-Turbulent Transition on a Rotating Wind Turbine Blade in the Free Atmosphere **2016**. *20,2*, 211–220.
21. de Luca, L.; Carlomagno, G.M.; Buresti, G. Boundary layer diagnostics by means of an infrared scanning radiometer. *Experiments in Fluids* **1990**, *9*, 121–128. doi:10.1007/BF00187411.
22. Gartenberg, E.; Roberts, A.S. Airfoil transition and separation studies using an infrared imaging system. *Journal of Aircraft* **1991**, *28*, 225–230. doi:10.2514/3.46016.
23. Dollinger, C.; Balaresque, N.; Sorg, M.; Fischer, A. IR thermographic visualization of flow separation in applications with low thermal contrast. *Infrared Physics & Technology* **2018**, *88*, 254–264. doi:https://doi.org/10.1016/j.infrared.2017.12.001.

24. Dollinger, C.; Sorg, M.; Balaresque, N.; Fischer, A. Measurement uncertainty of IR thermographic flow visualization measurements for transition detection on wind turbines in operation. *Experimental Thermal and Fluid Science* **2018**, *97*, 279–289. doi:10.1016/j.expthermflusci.2018.04.025.
25. Wolf, C.C.; Mertens, C.; Gardner, A.D.; Dollinger, C.; Fischer, A. Optimization of differential infrared thermography for unsteady boundary layer transition measurement. *Experiments in Fluids* **2019**, *60*. doi:10.1007/s00348-018-2667-0.
26. Gartenberg, E.; Roberts, A.S. Twenty-five years of aerodynamic research with infrared imaging. *Journal of Aircraft* **1992**, *29*, 161–171. doi:10.2514/3.46140.
27. Joseph, L.A.; Borgoltz, A.; Devenport, W. Infrared thermography for detection of laminar-turbulent transition in low-speed wind tunnel testing. *Experiments in Fluids* **2016**, *57*, 77. doi:10.1007/s00348-016-2162-4.
28. Montelpare, S.; Ricci, R. A thermographic method to evaluate the local boundary layer separation phenomena on aerodynamic bodies operating at low Reynolds number. *International Journal of Thermal Sciences* **2004**, *43*, 315–329. doi:10.1016/j.ijthermalsci.2003.07.006.
29. Crawford, B.K.; Duncan, G.T.; West, D.E.; Saric, W.S. Robust, automated processing of IR thermography for quantitative boundary-layer transition measurements. *Experiments in Fluids* **2015**, *56*, 149. doi:10.1007/s00348-015-2011-x.
30. Richter, K.; Schülein, E. Boundary-layer transition measurements on hovering helicopter rotors by infrared thermography. *Experiments in Fluids* **2014**, *55*, 1755. doi:10.1007/s00348-014-1755-z.
31. Dollinger, C.; Balaresque, N.; Gaudern, N.; Gleichauf, D.; Sorg, M.; Fischer, A. IR thermographic flow visualization for the quantification of boundary layer flow disturbances due to the leading edge condition. *Renewable Energy* **2019**, *138*, 709 – 721. doi:https://doi.org/10.1016/j.renene.2019.01.116.
32. XFOIL v6.99, https://web.mit.edu/drela/Public/web/xfoil/.
33. Mack, L.M. Transition and Laminar Instability. Technical Report NASA-CP-153203, JPL-PUBL-77-15, Jet Propulsion Laboratory, California Institute of Technology, Pasadena, California 91109, USA, 1977.
34. Mack, L.M. Boundary-Layer Linear Stability Theory. Technical Report 709, AGARD, Neuilly-sur-Seine, France, 1984.
35. Schülein, E. Experimental Investigation of Laminar Flow Control on a Supersonic Swept Wing by Suction. *AIAA-2008-4208, 4th Flow Control Conference, Seattle, Washington* **2008**.

Author Contributions: conceptualization, A.P.S. and T.R.; methodology, T.R and A.P.S; software, T.R. and A.P.S.; CFD, T.R. and A.P.S.; validation, T.R; formal analysis, T.R.; investigation, all; resources, C.D., N.B., E.S. and C.J.; data curation, T.R.; writing–original draft preparation, T.R., C.D. and A.P.S.; writing–review and editing, T.R., A.P.S. and A.F.; visualization, T.R., C.D., E.S.; supervision, A.P.S.; project administration, T.R.; funding acquisition, A.P.S.

Funding: "This research was funded by Gesellschaft für Energie und Klimaschutz Schleswig-Holstein GmbH, Kiel, Germany grant number 8/12-26"

Acknowledgments: We acknowledge help from Senvion, Denker & Wulf, wingtec and others. We thank the University of Oldenburg and Jaroslaw Puczylowski, PhD for using their wind tunnel for the calibration of the five hole probe. Computations were performed with resources provided by the North-German Superconducting Alliance (HLRN).

Conflicts of Interest: "The authors declare no conflict of interest."

Abbreviations

The following abbreviations are used in this manuscript:

AOA	angle of attack
BIMAQ	Bremer Institute for Metrology, Automation and Quality Science
CFD	Computational Fluid Dynamics
DLR	German Aerospace Center
DTC	Digital Temperature Compensation
DWGE	Deutsche WindGuard Engineering GmbH
L2D	lift-to-drag c_L/c_D
SCADA	Supervisory Control and Data Acquisition
SPL	sound pressure level
SS	steady-state phase
SSD	Solid state disk
SU	start-up phase
TI	turbulence itensity
TSR	tip-speed-ratio
WT	wind turbine